CHAPTER 4
RBS: EXPERIMENTAL RESULTS AND DISCUSSIONS

This thesis is based on three major experiments: namely, determination of detector solid angle by RBS spectra; determination of thickness and composition of thin films; and investigation of concentration of light elements in implanted heavy mass matrix.

4.1 Determination of detector solid angle by RBS spectra

RBS is often cited as a technique with 1% accuracy (Boudreault *et al.*, 2002); however, this depends on the accuracy of the information based on the product of the detector solid angle and the total number of ions incident on the sample or irradiation fluence (Boudreault *et al.*, 2002). Generally, the detector solid angle is in the range of 1 - 8 msr (Eloi *et al.*, 1995; Nurmela *et al.*, 2000). However despite the short sample-to-detector distance, an accurate direct measurement of the detector solid angle is actually not a simple and easy task. Trouble comes from either the geometry of the detector, or from obstacles inside the analysis chamber (which is normally packed with several components, such as a goniometer, stepper motors, sample holder, electron suppressor, collimator, detectors, etc.). Alternatively, RBS technique can serve as a useful supplement to quantify the value of its own detector solid angle.

4.1.1 Analytical procedure

The RBS mechanism is based on the nuclear elastic backscattering of a light incident ion from the nucleus of a target atom in the solid, as mentioned in detail in section 3.1. Within the same setup, two identical nuclei at different depths cause different backscattered energies. This is due to different encounters in low energy-transfer collisions along both the inward and outward trajectories, as illustrated in Figure 4.1. The backscattering yield of the edge in the RBS spectrum of Figure 4.1(b) corresponds to the scattering from the top surface of the sample. In theory, the yield from this region, which is designated as Y_1, can be calculated from the following

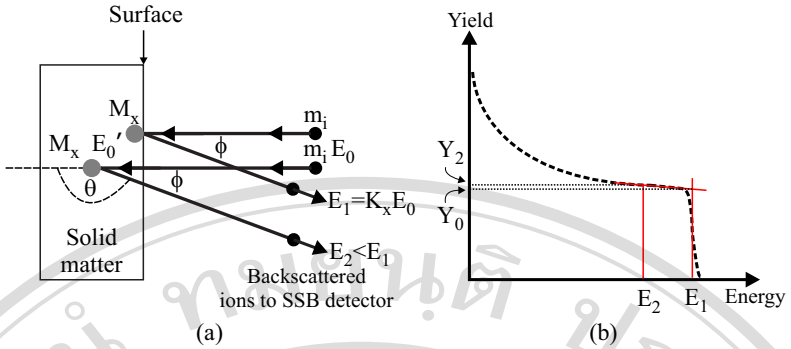

Figure 4.1. Illustration of the variables used in the equations. (a) Schematic drawing of RBS mechanism in pure solid matter of mass M_x when each of incident particles is ions of mass m_i with initial energy E_0. (b) The corresponding experimental energy spectrum of the backscattered ions as appeared on the MCA screen.

relationship (Vizkelethy, 1994) if the analyzing ion beam is incident normally to the target surface:

$$Y_1 = \sigma(E_0, \theta)\Omega Q \frac{\xi}{[\varepsilon(E_0)]}. \tag{4.1}$$

The equation of backscattering yield from collisions below the material surface (Y_2) is slightly different from Equation 4.1 due to energy loss, and can be expressed by Equation 3.41 or by

$$Y_2 = \sigma(E_0', \theta)\Omega Q \frac{\xi}{[\varepsilon(E_0')]} \frac{\varepsilon(KE_0')}{\varepsilon(E_2)}. \tag{4.2}$$

Here E_2 is the backscattered ion energy at the detector, while E_0' is the immediate ion energy before collision, which can be determined from the "energy loss ratio method" (Chu *et al.*, 1978):

$$E_0' = \frac{(E_2 + \alpha E_0)}{(K + \alpha)}, \tag{4.3}$$

where

$$\alpha \approx \frac{\varepsilon(KE_0)}{\varepsilon(E_0)} \frac{1}{\cos\phi}. \tag{4.4}$$

The ratio α of the energy lost along the outward track to that lost along the inward track is constant in the surface energy approximation. This method is accurate for the analysis of thin film spectra where the surface approximation holds.

Since determination of the top surface yield (Y_1) is usually troublesome due to the unclear edge position from the practical RBS spectrum, while Y_2 is more obvious, Y_1 is then determined from the relation between Y_1 and Y_2 derived from Equations 4.1 and 4.2:

$$Y_1 = Y_2 \left(\frac{E_0'}{E_0}\right)^2 \frac{[\varepsilon(E_0')]}{[\varepsilon(E_0)]} \frac{\varepsilon(E_2)}{\varepsilon(KE_0')}. \tag{4.5}$$

According to Equations 4.1 and 4.5, there is now only one unknown left to be calculated, i.e., detector solid angle (Ω).

4.1.2 Experimental details

Samples used in this investigation were 1×1 cm^2 pieces of pure C, Al, Ti, Fe, Cu, Mo and W, with thickness varying between 0.1-2.0 mm. Their surfaces were polished to a mirror-like finish. The seven samples with different mass and density were irradiated, at room temperature, by a 2.13-MeV He^{2+}-ion beam with a 1-mm spot size and a divergence of less than 0.05°. Backscattered particles from the samples were detected by three different SSB detectors of varying geometrics and sizes, as shown in Figure 4.2. The scattering angles were measured with an accuracy of 0.1° using a laser and high-precision channeling experiment goniometers.The sample-to-detector distances for detectors A, B and C were 136.40, 119.15 and 85.30 mm, respectively. Detectors B and C were used alternatively. During the measurement, the RBS chamber was under a vacuum pressure of 3×10^{-6} mbar.

To avoid overloading and pile-up effects, the samples were exposed only to a low beam current on the order of tens of nA. The temperature rise produced by such an irradiation at the surface of a sample was estimated to be only a few degrees, as shown in Figure 4.3. The surface temperature was obtained form the energy balance equation where the ion beam power input is equal to the emitted heat, according to

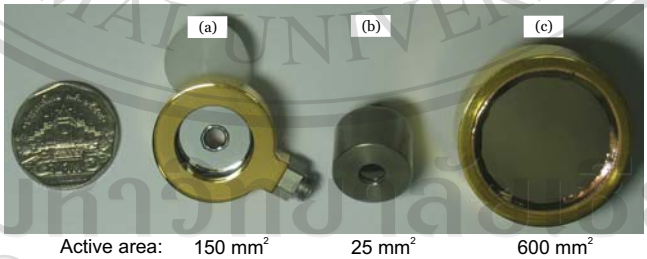

Figure 4.2. The geometry of three different SSB detectors. (a) A 150-mm^2 active area, including a 4-mm diameter hole, annular SSB detector which was placed at 180° with respect to the beam direction. (b) and (c) are 25-mm^2 and 600-mm^2 active areas, respectively, planar SSB detector which were placed at 166.2° with respect to the beam direction.

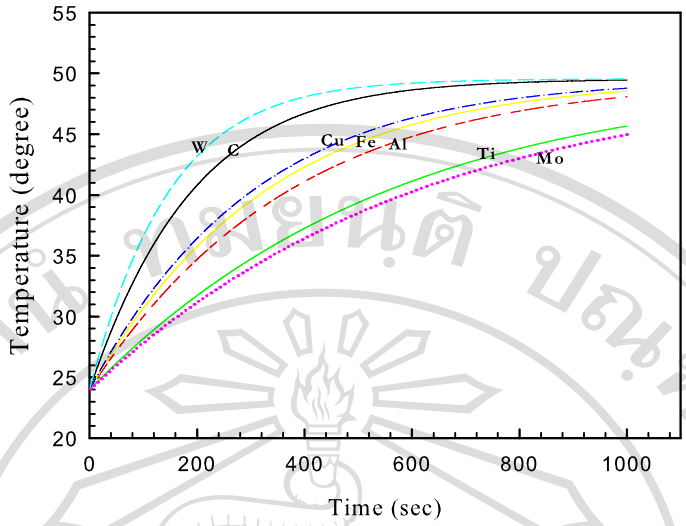

Figure 4.3. Estimation of the surface temperature when bombarded samples with 10 nA He^{2+}-ions at 2.13 MeV.

the Stefan-Boltzman law (Starling and Woodall, 1963):

$$\rho t C - \frac{dT}{dt} = \frac{P_{inp}}{A_s} - 2\sigma\varepsilon\left(T^4 - T_{surr}^4\right), \tag{4.6}$$

where ρ is the mass density of the sample, C is the specific heat capacity, t is the thickness, P_{inp} is the beam power input, A_s is the surface area, σ is the Stefan-Boltzman constant (5.67×10^{-8} W/m^{2}K^4), ε is the emissivity coefficient, and T_{surr} is the surrounding temperature.

4.1.3 Results and discussion

Figure 4.4 shows the RBS spectra from those seven sample types, measured by the three SSB detectors. From these spectra, the first step in quantification is to choose E_2, which paves the way to find Y_2. According to the concept of "surface energy approximation", which is used to approximate Equation 4.2, the selection of E_2 is restricted to a depth of less than 0.6 μm (Gyulai, 1980) from each sample surface. For a depth of about 0.2 μm in C, Al, Ti, Fe, Cu, Mo and W, the values of E_2 are 464, 1107, 1421, 1449, 1523, 1651, 1706 and 1793 keV, respectively. Their associated yields Y_2 are obtained from the spectra, as shown in Table 4.1. For the quantification of all ion beam techniques, stopping cross section data are of significant importance, and are given by Ziegler (1985). From the α values of 1.52, 1.27, 1.19, 1.16, 1.10, 1.11 and 1.04 (for C, Al, Ti, Fe, Cu, Mo and W, repectively) E_0' for each

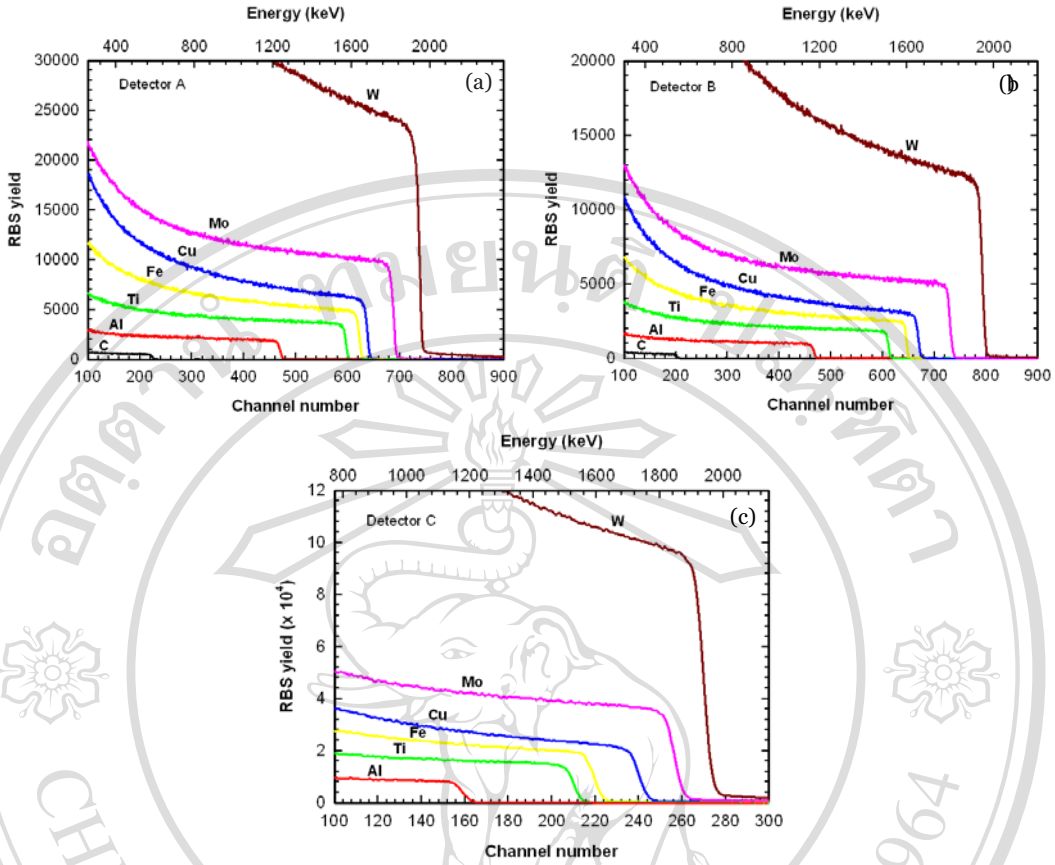

Figure 4.4. RBS spectra for 2.13-MeV He^{2+}-ions incident on pure slabs of C, Al, Ti, Fe, Cu, Mo and W, for normal incidence, detected by (a) detector A , (b) detector B and (c) detector C.

E_2 is obtained (Equation 4.3). Then, the value of surface yield Y_1 can be evaluated by using Equation 4.5, as shown in Table 4.1. The yield Y_0, which is found from extrapolating the yields in the spectrum to energy KE_0, as shown in Figure 4.1(b), is also shown in this table. The values of the detector solid angle are then calculated from Equation 4.1 by assuming that the collected charge is accurate, as shown in Table 4.2.

In order to check the accuracy of the results, another approach was also tried: fitting the experimental spectra to the SIMNRA code simulated spectra. The extracted values of the detector solid angle are also presented in Table 4.2. The correctness of these values can be verified by comparison with the values obtained from direct geometrical measurements (i.e., $\Omega = A/R^2$, where A is the detector area and R is the sample-to-detector distance). For the value of sample-to-detector distance, thickness of the samples was considered; so the value of the detector solid angle for

Table 4.1. Comparison of backscattering yields of the RBS spectra obtained from different detectors and samples. Y_2: the measured yield from the depth of 200 nm; Y_1: the calculated yield from Equation 4.5; Y_0: the extrapolated yield at energy KE_0.

Sample	Y_2 counts/channel	Y_1 counts/channel	Y_0 counts/channel
Detector A (annular detector: 150 mm^2 active area with energy resolution of 19 keV)			
C	556	527	497±25
Al	1850	1824	1924±55
Ti	3606	3541	3596±79
Fe	4709	4541	4793±85
Cu	6317	6025	6083±94
Mo	9450	9113	9754±128
W	25089	23841	23092±190
Detector B (planar detector: 25 mm^2 active area with energy resolution of 12 keV)			
C	305	290	260±18
Al	996	976	972±36
Ti	1908	1861	1848±44
Fe	2503	2402	2445±57
Cu	3354	3197	3001±79
Mo	5004	4824	4990±100
W	13131	12527	11902±126
Detector C (planar detector: 600 mm^2 active area with energy resolution of 45 keV)			
Al	7636	7482	7899±138
Ti	14520	14166	14787±144
Fe	18504	17758	18906±152
Cu	24870	23704	21980±165
Mo	37680	36324	35703±257
W	98430	93900	93494±380

each sample, from a direct geometrical measurement, was somewhat different. The ratio shown in Table 4.2 is the detector solid angle ratio of the angle obtained by this *in situ* RBS method, or SIMNRA simulation approach and that obtained from direct geometrical measurement. This data set of both the manual method and SIMNRA simulation shows that the ratio is very close to unity. The data of all detectors determined from Y_1 show the best results, with ∼0.9% variation. Particularly snice this method is an *in situ* approach, one can conveniently determine the basic parameter

Table 4.2. Comparison of the detector solid angle values of the 3 detectors evaluated from 4 different methods which are direct geometrical measurement, *in-situ* determination from yields Y_1 and Y_0, and SIMNRA simulation fitting. The ratio columns represent values obtained by dividing a calculation or simulation value with a directly measured value.

Sample	Geometrical measurement	Calculation (from Y_1)		Calculation (from Y_0)		SIMNRA	
		Ω (msr)	ratio	Ω (msr)	ratio	Ω (msr)	ratio
Detector A (annular detector: 150 mm^2 active area with energy resolution of 19 keV)							
C	7.50±0.02	7.44±0.35	0.99	6.92±0.35	0.92	7.67	1.02
Al	7.53±0.02	7.50±0.26	1.00	7.92±0.23	1.05	7.86	1.04
Ti	7.61±0.02	7.63±0.21	1.00	7.75±0.17	1.02	7.86	1.03
Fe	7.47±0.02	7.56±0.19	1.01	7.98±0.14	1.07	8.00	1.07
Cu	7.47±0.02	7.43±0.17	0.99	7.50±0.12	1.00	7.58	1.01
Mo	7.61±0.02	7.66±0.17	1.01	8.20±0.11	1.08	7.94	1.04
W	7.39±0.02	7.32±0.14	0.99	7.09±0.06	0.96	7.47	1.01
Mean			1.00		1.01		1.03
Coefficient of variation(%)			0.81		5.67		1.96
Detector B (planar detector: 25 mm^2 active area with energy resolution of 12 keV)							
C	1.79±0.03	1.79±0.11	1.00	1.61±0.11	0.90	1.75	0.98
Al	1.80±0.03	1.79±0.07	0.99	1.78±0.07	0.99	1.74	0.97
Ti	1.82±0.03	1.80±0.05	0.99	1.79±0.04	0.98	1.79	0.98
Fe	1.79±0.03	1.80±0.05	1.01	1.83±0.04	1.02	1.83	1.02
Cu	1.78±0.03	1.78±0.04	1.00	1.67±0.04	0.94	1.73	0.97
Mo	1.82±0.03	1.84±0.04	1.01	1.90±0.04	1.04	1.84	1.01
W	1.76±0.03	1.75±0.03	0.99	1.66±0.03	0.94	1.71	0.97
Mean			1.00		0.97		0.99
Coefficient of variation(%)			0.79		5.17		2.19

Ω for RBS analysis. Because the detector solid angle is a constant of the apparatus setup, while the product of the detected charge and the detector solid angle is actually measured during RBS analysis, the apparent variations in the detector solid angle values shown in Table 4.2 are actually variations in the collected charge. Therefore the measured values in Table 4.2 also indicate reproducibility of the measurement of the charge collection.

Table 4.2. Continued

Sample	Geometrical measurement	Calculation (from Y_1)		Calculation (from Y_0)		SIMNRA	
		Ω (msr)	ratio	Ω (msr)	ratio	Ω (msr)	ratio
Detector C (planar detector: 600 mm^2 active area with energy resolution of 45 keV)							
Al	85.03±0.32	86.32±1.60	1.02	91.47±1.73	1.08	90.29	1.06
Ti	86.57±0.32	86.35±0.88	1.00	90.47±1.20	1.05	88.50	1.02
Fe	84.03±0.32	83.73±0.72	1.00	89.47±0.95	1.06	87.93	1.05
Cu	83.93±0.32	82.92±0.62	0.99	87.18±0.74	0.92	78.61	0.94
Mo	86.57±0.32	87.04±0.58	1.01	85.87±0.56	0.99	83.88	0.97
W	82.56±0.32	82.54±0.33	1.00	82.48±0.22	1.00	83.88	1.02
Mean			1.00		1.02		1.01
Coefficient of variation(%)			0.92		5.73		4.71

4.1.4 Summary

An *in situ* method of the determination of the detector solid angle by using the RBS spectrum itself has been proposed. This method has been shown to provide information on the detector solid angle with the highest accuracy, in a single fast measurement, and independent of the simulation program. It is promising and practically applicable, especially for detectors and RBS measurement setups with complex geometries.

4.2 Depth resolution

As depth profiling is one of the key performances of the RBS technique, depth resolution is an important parameter to be thoroughly known. Depth profiling refers to the ability to sense composition changes with depth or variations in impurity distribution with depth. Several factors can be the cause the depth resolution, such as beam energy, scattering angle and the total charge. The effect of these factors on the depth resolution will be discussed.

The RBS depth resolution δx is defined by (Chu *et al.*, 1997)

$$\delta x = \frac{\delta E}{[S]}, \tag{4.7}$$

where δE is the total energy resolution, and $[S]$ is energy loss factor. This expression shows that the best depth resolution is achieved when the energy resolution is kept

at minimal value but vice versa for the energy loss factor.

To evaluate Equation 4.7, the contributions to δE must be identified and determined. They are the system resolution δE_r and the energy straggling δE_s. The system resolution is normally stemming from the detector intrinsic energy resolution and from geometrical broadening due to beam divergence and finite acceptance angle of the detector. Assuming they are uncorrelated and can be characterized by a Gaussian distribution, these factors add up in quadrature:

$$(\delta E)^2 = (\delta E_r)^2 + (\delta E_s)^2. \tag{4.8}$$

In practical, the energy resolution δE is defined by the energy width between the positions at 12% and 88% of the full height of a signal that corresponds to an abrupt change in sample composition (Chu *et al.*,1978). Figure 4.5 shows the influence of the system resolution δE_r and of the energy straggling δE_s for the high- and low-energy edges of the RBS spectrum of 2.1-MeV He^{2+}-ion backscattered from a 405 nm thick SnO_2 film on Si substrate. The energy resolution is 33 keV at the surface and slowly increases to 57 keV at a depth of 405 nm. The energy δE of the high-energy edge gives the depth resolution δE at the surface, which is dominated by the system resolution δE_r. From Figure 4.5, δE = 33 keV and hence δE_r = 33 keV. The energy

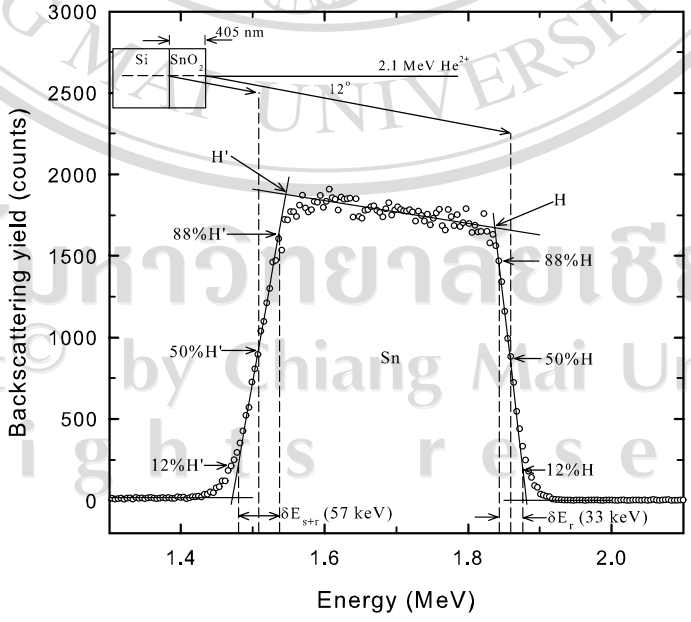

Figure 4.5. Depth resolution for RBS of 2.1-MeV He^{2+}-ions backscattered from 405 nm of SnO_2 film deposited on a Si substrate.

loss factor $[S_0]_{Sn}^{SnO_2}$ is 82.4 eV/Å in the surface approximation, so that the depth resolution at the surface is $\delta x = 40$ nm, as determined by Equation 4.7.

For low-energy edge, the energy δE is larger because of the added effect of energy straggling in He^{2+}-ion that have to penetrate in and out of the film. From Figure 4.5, $\delta E = 57$ keV and hence $\delta x = 67$ nm, where the energy loss factor $[S]_{Sn}^{SnO_2}$ is 82.45.3 eV/Å as the energy loss of He^{2+}-ion in traversing the SnO_2 film is taken into account. At this depth, the contribution of the energy straggling to δE, as determined by Equation 4.8, is $\delta E_s = 46.5$ keV.

The depth resolution can be improved by increasing energy loss factor $[S]$ as shown in Equation 4.7. There are three ways to maximize $[S]$. First, the $[S]$ can be greatly increased by increasing the path length of the incident ion in the sample. This is accomplished by tilting the sample normal relative to the incoming beam, i.e., grazing beam incidence and/or exit. The second way to maximize $[S]$ is by decreasing energy of the incident ions, which causes (dE/dx) to decrease (cf. Equation 3.10). However, the trade-off here is that at lower beam energies there is a decrease in depth that is accessible. Finally, increasing the atomic number of the projectile will also increase energy loss factor $[S]$. This modification increases the kinematic factor (cf. Equation 3.4) and also leads to higher (dE/dx) (cf. Equation 3.10).

4.3 Thickness and composition of thin films

RBS technique is widely used in the investigation of thicknesses of thin films, multi-elemental or multi-layer thin films, and also in the determination of their composition. In this thesis, the determinations of thickness and composition for Cu/Ag multilayer films, and amorphous indium tin oxide films are presented.

4.3.1 Cu/Ag multilayer films

Figure 4.6 shows an energy spectrum of 2.12-MeV $^4He^{2+}$-ions backscattered from a Cu/Ag multilayer film on Si substrate. The beam current is 15 nA with a total charge of 20 μC. The film consists of 60 bilayers of Cu/Ag, and was prepared by thermal evaporation from a tungsten boat onto a well-cleaned Si wafer substrate at room temperature under a vacuum of 2×10^{-4} mbar. As shown in Figure 4.6, the backscattering peaks of Cu and Ag are overlapping. Since each layer is so thin, the peaks from each individual layer are not resolved by the detection system. The

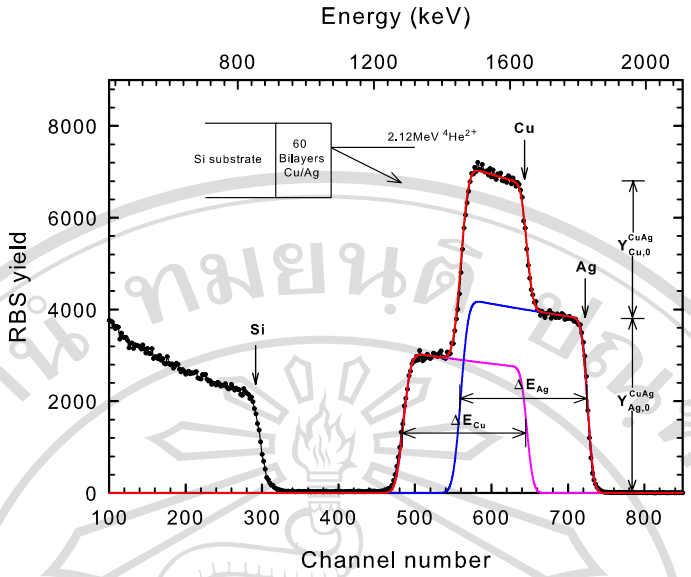

Figure 4.6. The 2.12-MeV He^{2+} RBS spectrum of Cu/Ag multilayer (60 bilayers) film on Si substrate. The backscattering peaks of Cu and Ag are overlapping. The solid lines are the computer-assisted peak separation of overlapping peaks.

detector energy resolution is 12 keV, which is six times larger than the energy loss in each layer. As seen in Figure 4.6, the backscattering spectrum of Cu and Ag are quite smooth, indicating that the mixture of Cu and Ag is uniform throughout the film. Therefore the film can be treated as a compound film of Cu_mAg_n.

The evaluation of the stoichiometry of the film is first calculated by the surface spectrum heights method. This method is described in subsection 3.1.5.2. Figure 4.6 shows the spectral step heights of Cu and Ag signals. The signal surface heights are designated as $Y^{CuAg}_{Cu,0}$ and $Y^{CuAg}_{Ag,0}$ for Cu and Ag, respectively. The data from Figure 4.6 are given in Table 4.3.

For the first iteration, which is the start of a zeroth-order analysis, Equation 3.57 with the $[\varepsilon_0]$ ratio taken as unity is used. The stoichiometric ratio, m/n, is then

$$\frac{m}{n} = \frac{N^{CuAg}_{Cu}}{N^{CuAg}_{Ag}} = \frac{(2705 \pm 30)}{(3709 \pm 30)} \cdot \frac{2.618}{0.992} \cdot \frac{0.992}{0.996} = 1.876 \pm 0.026.$$

The values of the stopping cross section factor are then computed by using Equations 3.32 and 3.33, with $m/n = 1.876$:

$$[\varepsilon_0]^{CuAg}_{Cu} = 141.460 \times 10^{-15}\text{eV cm}^2 \quad ; \quad [\varepsilon_0]^{CuAg}_{Ag} = 145.358 \times 10^{-15}\text{eV cm}^2.$$

Finally, from Equation 3.57, the stoichiometric ratio m/n is 1.829 ± 0.029. If the

molecular formula for the film is denoted as Cu_mAg_n, then $m = 0.647 \pm 0.004$, and $n = 0.353 \pm 0.004$. The quoted uncertainties are statistical due to the uncertainty in the $Y_{i,0}$ ratio.

For a uniform two-element film, the energy width can be used to determine elemental areal densities. This method is described earlier in subsection 3.1.5.3. The parameter values directly associated with the spectrum shown in Figure 4.6 are listed in Table 4.3. By using Equation 3.60, the stoichiometric ratio is

$$\frac{m}{n} = \frac{N_{Cu}^{CuAg}}{N_{Ag}^{CuAg}} = \frac{(2705 \pm 30)}{(3709 \pm 30)} \cdot \frac{2.618}{0.992} \cdot \frac{0.992}{0.996} \cdot \frac{(364 \pm 3)}{(378 \pm 3)} = 1.810 \pm 0.036.$$

The areal densities $(Nt)_{Cu}$ and $(Nt)_{Ag}$, when using the surface energy approximation, are then computed by using Equation 3.59 with $m/n = 1.810$. Finally we get $(Nt)_{Cu}^{SEA} = (1.653 \pm 0.022) \times 10^{18}$ atoms/cm^2 and $(Nt)_{Ag}^{SEA} = (0.913 \pm 0.016) \times 10^{18}$ atoms/cm^2. The energy loss of the $^4He^{2+}$-ion in the film is calculated using Equation 3.46, i.e.,

$$\Delta E_{in}^{SEA} = (66.061 \times 10^{-15})(1.653 \times 10^{18}) + (90.973 \times 10^{-15})(0.913 \times 10^{18}) = 192 \quad \text{keV},$$

so the mean $^4He^{2+}$-ion energy is (Equations 3.47),

$$\bar{E} = 2120 - \frac{192}{2} = 2024 \quad \text{keV}.$$

Table 4.3. Data extracted from Figure 4.6 with backscattering parameters based on the surface energy approximation.

Data	Parameters
$Y_{Cu,0}^{CuAg} = 2705 \pm 30$ counts	$\sigma_R^{Cu}(E_0, 166°) = 0.992 \times 10^{-24}$ cm^2
$Y_{Ag,0}^{CuAg} = 3790 \pm 30$ counts	$\sigma_R^{Ag}(E_0, 166°) = 2.618 \times 10^{-24}$ cm^2
$\Delta E_{Cu} = 364 \pm 3$ keV	$(\sigma/\sigma_R)_{Cu} = 0.996$
$\Delta E_{Ag} = 378 \pm 3$ keV	$(\sigma/\sigma_R)_{Cu} = 0.992$
$A_{CuAg} = 1133310 \pm 1324$ counts	$K_{Cu} = 0.7797$ $K_{Cu} \times E_0 = 1653$ keV
$A_{Cu} = 467859 \pm 2180$ counts	$K_{Ag} = 0.8636$ $K_{Ag} \times E_0 = 1831$ keV
$A_{Ag} = 664942 \pm 2550$ counts	$\varepsilon^{Cu}(2120 \text{ keV}) = 66.061 \times 10^{-15}$ eV cm^2
DTR = 1.02	$\varepsilon^{Cu}(1831 \text{ keV}) = 68.955 \times 10^{-15}$ eV cm^2
	$\varepsilon^{Cu}(1653 \text{ keV}) = 70.705 \times 10^{-15}$ eV cm^2
	$\varepsilon^{Ag}(2120 \text{ keV}) = 90.973 \times 10^{-15}$ eV cm^2
	$\varepsilon^{Ag}(1831 \text{ keV}) = 96.134 \times 10^{-15}$ eV cm^2
	$\varepsilon^{Ag}(1653 \text{ keV}) = 99.488 \times 10^{-15}$ eV cm^2

This mean energy should be used in the evaluation of the $[\varepsilon]_{Cu}^{CuAg}$ and $[\varepsilon]_{Ag}^{CuAg}$ factors, which are consecutively used to obtain more accurate values of $(Nt)_{Cu}$ and $(Nt)_{Ag}$. The areal densities in the mean energy approximation are $(Nt)_{Cu}^{MEA} = (1.630 \pm 0.022) \times 10^{18}$ atoms/cm^2 and $(Nt)_{Ag}^{MEA} = (0.901 \pm 0.016) \times 10^{18}$ atoms/cm^2.

One of the procedures that can be used to analyze the spectrum shown in Figure 4.6 is computer fitting to separate the contributions from the Cu and Ag signals. This fitting procedure is applicable to films that have uniform composition. The results of the fitting provide the integrated peak counts A_{Cu} and A_{Ag} for use in peak integration analysis procedure. This method has been described in subsection 3.1.5.1. The values of the total integrated counts, A_{CuAg}, and the fitting procedure provide the integrated counts A_{Cu} and A_{Ag} as listed in Table 4.3. The areal densities $(Nt)_{Cu}$ and $(Nt)_{Ag}$ in the surface energy approximation are then computed by using Equation 3.45. Finally we get $(Nt)_{Cu}^{SEA} = (1.797 \pm 0.008) \times 10^{18}$ atoms/cm^2 and $(Nt)_{Ag}^{SEA} = (0.972 \pm 0.004) \times 10^{18}$ atoms/cm^2.

Thus the mean energy of the $^4He^{2+}$-ion in the film is 2017 keV. The areal densities including the correction for energy loss in the film are $(Nt)_{Cu}^{MEA} = (1.627 \pm 0.007) \times 10^{18}$ atoms/cm^2 and $(Nt)_{Ag}^{MEA} = (0.880 \pm 0.004) \times 10^{18}$ atoms/cm^2. The average stoichiometric ratio for this film is 1.849 ± 0.011.

For uniform composition film, a combination of the energy width and peak integration methods can also be used to obtain the areal densities. Through the use of Equation 3.61, the integrated peak counts are $A_{Cu} = 461634 \pm 4900$ and $A_{Ag} = 671676 \pm 4900$. Substitution of these values into Equation 3.37, along with the mean energy approximation, provides $(Nt)_{Cu} = (1.605 \pm 0.017) \times 10^{18}$ atoms/cm^2, $(Nt)_{Ag} = (0.889 \pm 0.012) \times 10^{18}$ atoms/cm^2 and $m/n = 1.805 \pm 0.023$.

However, the simplest method for the analysis of a thin film, as in Figure 4.6, is by generating a spectrum with fully separated peaks, so the peak integration method can be applied in a straightforward manner. Figure 4.7 shows a 4.52-MeV $^4He^{2+}$-ions backscattering spectrum of the same film shown in Figure 4.6. The backscattering peaks for Cu and Ag have no overlapping part. The total charge, Q, is 14 μC and the dead-time-ratio (DTR) factor is 1.01. The ^{4}He-Cu and ^{4}He-Ag cross sections are still in keeping with Rutherford's formula at this energy. On the other hand, the ^{4}He-Si cross section is not of a Rutherford type at the higher energy; there are resonances near channels 240 and 350, but analysis of the substrate is not of interest in this case. The spectrum provides the integrated peaks counts of $A_{Cu} = 70792 \pm 321$ and $A_{Ag} = 99919 \pm 365$. Substitution of these values into Equation 3.45,

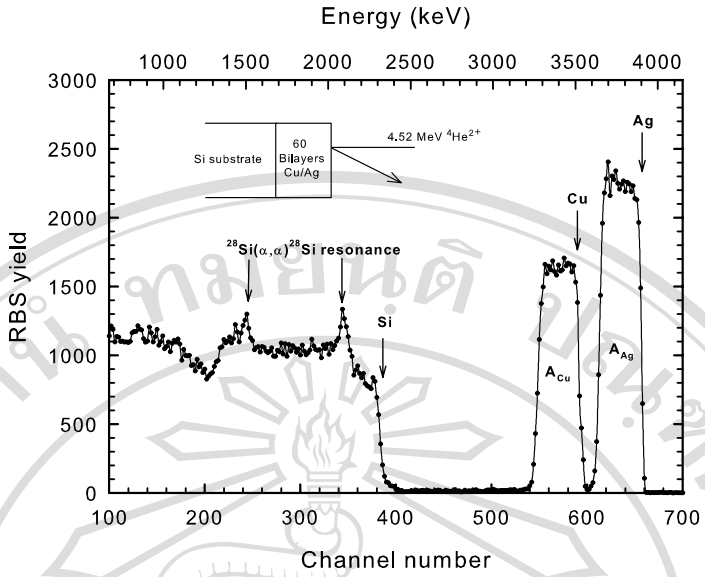

Figure 4.7. The 4.52-MeV He^{2+}-ions RBS spectrum of Cu/Ag multilayer (60 bilayers) film on Si substrate. The backscattering peaks for Cu and Ag are fully separated.

along with the mean energy approximation, provides $(Nt)_{Cu} = (1.693 \pm 0.008) \times 10^{18}$ atoms/cm^2, $(Nt)_{Ag} = (0.906 \pm 0.003) \times 10^{18}$ atoms/cm^2 and $m/n = (1.868 \pm 0.011)$.

For convenience, results from various methods used, as mentioned above, are compared in Table 4.4. The use of the peak integration method – with both the computer-assisted separation of overlapping Cu and Ag peaks, and the fully separated peaks – produces results of the highest accuracy, by about 0.5%. However, it is not always possible to produce spectra whose peaks are fully separated. If the film composition is uniform, then computer-assisted peak separation of overlapping peaks can be used. The use of the energy width method produces results of inferior accuracy by about 2% because this method depends on the accuracy of the stopping cross section factor. However, this method can be done by hand for the case of overlapping peaks. The combination of the energy width and peak integration methods produces results with an accuracy comparable to the energy width method.

The physical film thickness (t) can be calculated by using Equations 3.50 and 3.51 if the density of the film is known. But for a synthesized film, this is normally an unknown parameter. It is customarily estimated from the elemental bulk density. The values of elemental bulk densities for Cu and Ag are $N_{Cu} = 8.483 \times 10^{22}$ atoms/cm^3 and $N_{Ag} = 5.845 \times 10^{22}$ atoms/cm^3, respectively. Hence the thickness of the film is about 346 nm.

Table 4.4. Comparison of the results of the Cu/Ag multilayer film obtained from various methods.

Method	m	n	$(Nt)_{Cu}$	$(Nt)_{Ag}$
Stoichiometry by spectrum height	0.647±0.004	0.353±0.004	-	-
Energy width method (with spectrum heights)	0.644±0.005	0.356±0.005	1.630±0.022	0.901±0.016
Peak integration method (with computer-assisted separation of overlapping Cu and Ag peaks)	0.649±0.001	0.351±0.001	1.627±0.007	0.880±0.004
Combination of energy width and peak integration method	0.644±0.003	0.356±0.003	1.605±0.017	0.889±0.012
Peak integration method (with fully separated peak data)	0.652±0.001	0.348±0.001	1.693±0.008	0.906±0.003

$(Nt)_i$ values are in units of 10^{18} atoms/cm^2

4.3.2 Amorphous indium tin oxide (ITO) films

Tin-doped indium oxide (ITO) is of great importance in technology, and has been used in a wide variety of fields for the creation of products such as opto-electronic devices (Mattox, 1991), photovoltaic solar cells (Bellingham *et al.*, 1991), electrochromic devices (Pankove, 1980), liquid crystal displays (Osaza *et al.*, 1994), heat-reflecting mirrors (Copra and Das, 1983), sensors (Takada *et al.*, 1995), etc. Over the past decades, much research effort has been devoted to the preparation of ITO films, since they are involved in such diverse applications. Consequently various manufacturing techniques, such as reactive electron vaporation (Rauf, 1996), DC and RF magnetron sputtering (Shigesato and Paine, 1994), reactive thermal deposition (Thilakan *et al.*, 1995), laser ablation (Cali *et al.*, 1998), and spray pyrolysis (Jang *et al.*, 2006), have been successfully developed. This thesis reports on an effective approach to producing ITO films by DC and RF magnetron sputtering in water vapor atmosphere.

Amorphous indium tin oxide thin films were deposited by DC+RF magnetron sputtering using an ITO target (95 wt.% In_2O_3; 5 wt.% SnO_2) at room temperature. The system was evacuated using a turbomolecular pump to a base pressure

of approximately 5×10^{-7} Torr. The films were deposited at a gas pressure of 8×10^{-3} Torr in water vapor atmospheres ($0 - 6 \times 10^{-5}$ Torr) with a total sputtering power of 135 W. The Ar flow rate (50 sccm) was kept constant either with or without water introduction.

Figure 4.8 shows the RBS spectra together with the SIMNRA fits for those ITO films. Raw RBS data were collected using 2.1-MeV He^{2+}-ions with beam current

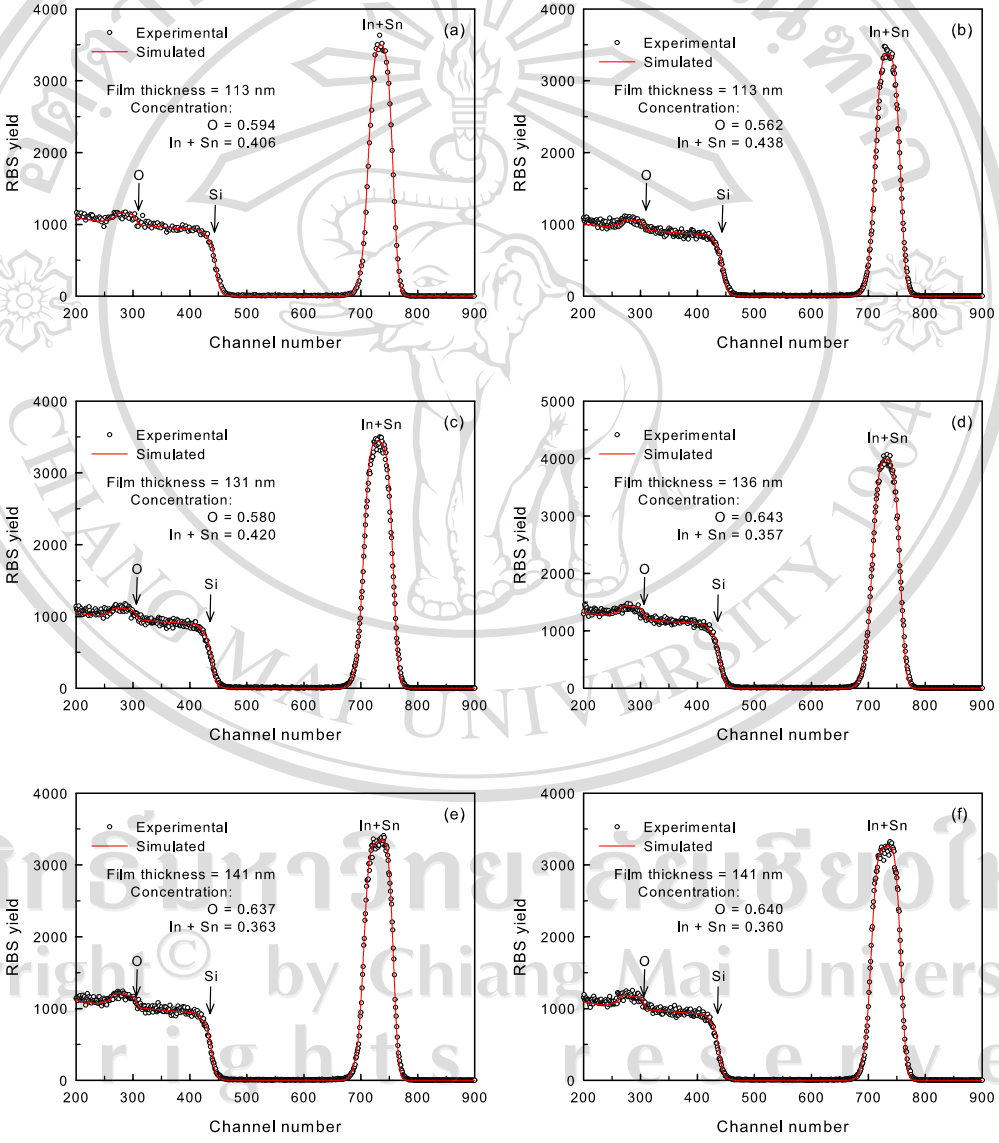

Figure 4.8. 2.1-MeV He^{2+}-ions RBS spectra with the SIMNRA fits for the ITO films on Si substrate deposited at water vapor partial pressures of (a) 0, (b) 1×10^{-5}, (c) 2×10^{-5}, (d) 3×10^{-5}, (e) 5×10^{-5} and (f) 6×10^{-5} Torr.

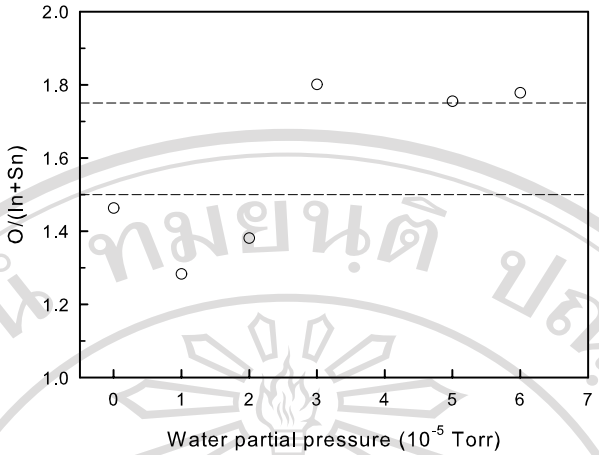

Figure 4.9. Oxygen to indium and tin ratios [O/(In+Sn)] of ITO films deposited at different water vapor partial pressures.

of 10 nA. The spectra represent the backscattering from In and Sn targets by a single peak, since the atomic masses of these two elements are very close, i.e., $M_{In} = 115$ and $M_{Sn} = 119$. The energy difference in the backscattering spectrum is 8 keV, but the detector energy resolution is 12 keV. Therefore the peaks from both elements are not resolved by the detection system.

Oxygen to indium-and-tin ratios [O/(In+Sn)] obtained from these ITO films are shown in Figure 4.9. The values are scattered around 1.5 (the stoichiometric ratio for In_2O_3) or less (indicating oxygen deficiency) for the films deposited at low water-vapor partial pressures (2×10^{-5} Torr or lower). The values increased abruptly to a constant value (approximately 1.75) at high water-vapor partial pressures (3×10^{-5} Torr or higher).

4.3.3 Summary

The examples shown in this subsection illustrate how RBS analysis can be used to provide quantitative analysis of the thickness, and stoichiometric composition of thin films. By referring to known Rutherford cross sections, stopping cross sections and the experimental parameters of the scattering geometry, the investigation can be done by hand – especially in cases when the backscattering peaks from the elements in a compound film are fully separated. Moreover, the investigation can be done using the well-known SIMNRA simulation program.

4.4 Concentration of light elements in implanted heavy mass matrix

In this thesis, the determination of the depth profile of C-ion implanted Si substrate, for the purpose of analysis of ion beam synthesized SiC, is presented. Two types of C-ion implantation are considered, i.e., single-energy and multi-energy C-ion implantation.

4.4.1 Single-energy C-ion implantation

Two types of C-ion implantation into Si crystalline substrate were carried out. The first type was the implantation of relatively low single-energy, 40-keV or 80-keV, $^{12}C^{+}$-ions with fluences of 6.5×10^{17} and 2.7×10^{17} ions/cm^2, respectively, using conventional 200-keV analyzed-beam ion implanters. The second type was performed with a 1.7-MV HVEE tandem Tandetron accelerator by using medium-energy 300-keV $^{12}C^{+}$-beams extracted from a Cs sputter ion source. The fluences of C-ions range from 5.2×10^{17} to 2.6×10^{18} ions/cm^2.

The correctness of the RBS-profile calculation program was first tested on the sample implanted by 40-keV and 80-keV carbon ions. Figure 4.10 shows the random RBS spectra of the unimplanted sample and the samples implanted by 40-keV and 80-keV carbon ions. The existence of implanted carbon ions results in a clear decrease of the RBS yield from Si near the surface edge. The RBS yield from the carbon atoms themselves is visible at around channel number 160 and 240, although due to the low carbon cross section it is very indistinct. The evaluation of the carbon profile is more precise if the silicon part of the spectra is used. It is clearly seen that the silicon yield of the surface layer decreases with increasing the carbon fluence.

Figure 4.11 shows the C-ion depth profiles extracted from these RBS spectra. Simulated profiles from four computer codes: SRIM, SIIMPL, DataFurnace and SIMNRA, are also included for comparison. The RBS-measured depth profile was smoothed using an eight-point adjacent averaging method, as shown in the inset of Figure 4.11. The mean range of the RBS-measured profile, about 265 nm for 80-keV C-ion implantation, is in good agreement with the other calculations, e.g., about 255 nm using SRIM (this simulation program assumes the target is an amorphous material). As SIIMPL takes the channeling effect into account, the SIIMPL-simulated profile exhibits a slightly deeper distribution of the C-ions; thus the mean range is about 270 nm. As shown in Figure 4.11, the depth profiles obtained from SIMNRA and DataFurnace are given in fairly rough form. Using SIMNRA or DataFurnace for

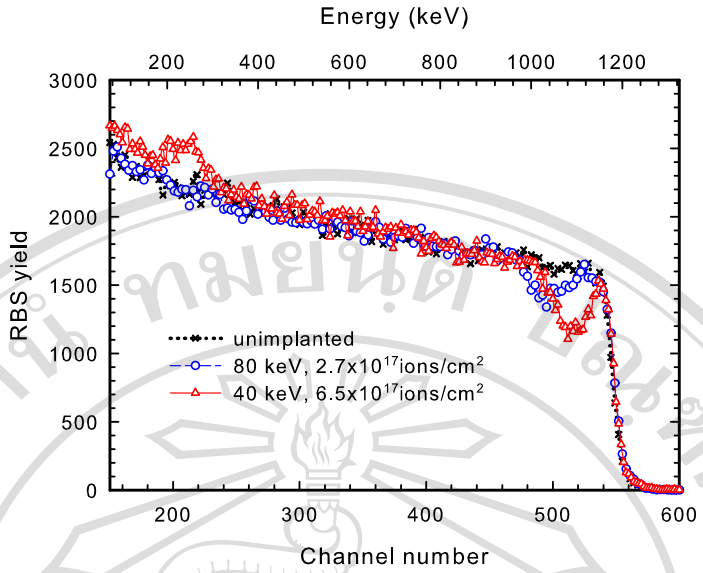

Figure 4.10. 2.1-MeV He^{2+}-ions RBS spectra of (100) silicon wafers implanted with C ions of 6.5 $\times$ 10^{17} ions/cm^2 at 40-keV and 2.7 $\times$ 10^{17} ions/cm^2 at 80-keV. It is obvious that the dips on the right are far better than the peaks on the left according to the accuracy of the extracted carbon depth profiles. The RBS spectrum from the unimplanted Si wafer is also shown.

elemental depth profiles is basically a fitting process. Normally in fitting procedure, the user should assign the numbers of sample layers, the thickness and the concentration in each layer, followed by simulation or calculation to generate a result that has the best fit with the least deviation from the experimental data. The extracted depth profile depends on this information. For successful fitting, experience in both the relevant physics of the materials investigated, and computer code operation, is usually necessary helpful. However, this method directly utilizes the measured RBS spectra of Y_A^{AB} and Y_A^{pure} (cf. Equations 3.39 and 3.41) with the database of stopping cross sections and the kinematic factor for a straightforward generation of the final result with detailed information. Furthermore, with certain approximation, simple deconvolution can be done on the extracted elemental depth profile to obtain more realistic information.

From these measurements, there are depth profiles with two different implanted doses. It is possible to estimate the limitation of the RBS method for determining a lighter-impurity distribution in a heavier matrix. It is assumed that the relative difference in the RBS yield of the matrix between the virgin and the ion-implanted samples at the maximum in the silicon deficiency region is linearly

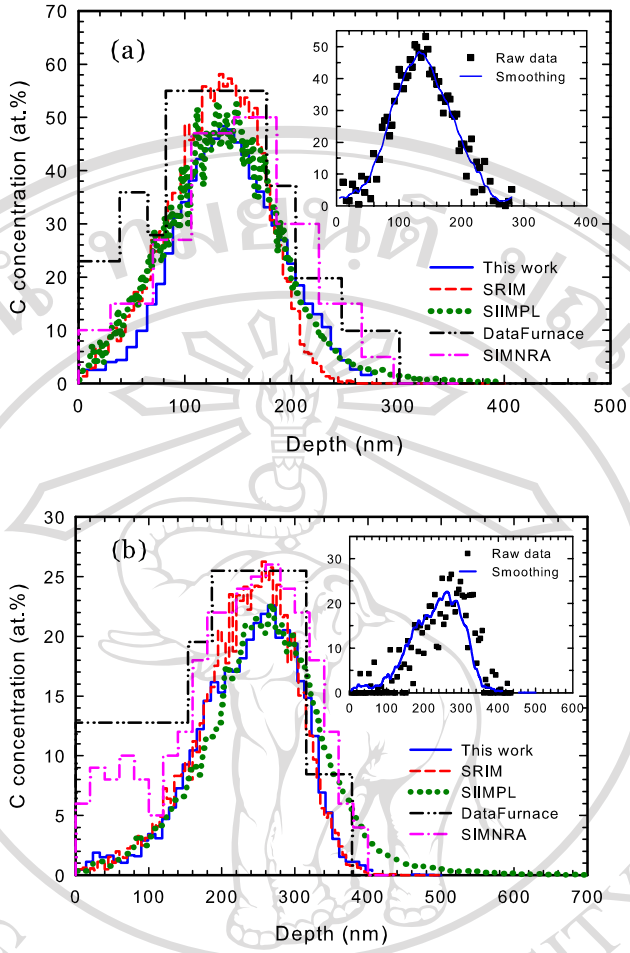

Figure 4.11. Depth profiles of as-implanted C-ions in silicon wafers as determined by RBS method, DataFurnace and SIMNRA codes and simulations done by SRIM and SIIMPL programs. The implantation conditions are (a) 6.5×10^{17} ions/cm^2 at 40-keV, and (b) 2.7×10^{17} ions/cm^2 at 80-keV. The inset shows the RBS-analyzed raw depth profiles and the smoothed profile.

proportional to the ion fluence Φ. Thus, there is the expression

$$\Delta_Y = a\Phi + b, \tag{4.9}$$

where Δ_Y represents the relative RBS yield difference. This is defined as $(Y_v - Y_i)/Y_v$ with Y_v equal to virgin yield and Y_i equal to yield from the implanted sample extracted from the channel number corresponding to the lowest yield from the Si-deficiency region. From the RBS spectra with different fluences in Figure 4.10, constants a and b in Equation 4.9 can be determined. The fluence limit, Φ_{limit}, can be estimated from Equation 4.9. If the minimum Δ_Y is set to be the mean relative noise of an RBS

spectrum, in which the yield difference is a mean difference between high and low yields of the spectrum, the minimum Φ can be estimated. For this practical case, the minimum Δ_Y is observed to be about 1/15; hence Φ_{limit} is around 5×10^{16} ions/cm^2, which means that when the fluence is 5×10^{16} ions/cm^2 or lower, the Si-deficiency region of the spectrum is merged in the yield noise. This discussion implies that this RBS method will overlook fluences lower than about 5×10^{16} ions/cm^2 of lighter ions implanted in a heavier matrix. Therefore, if this limit fluence is added to the measured fluence from the RBS profile, the final fluence is almost the same as that theoretically predicted.

For 300-keV C-ion implantation, the RBS spectra are shown in Figure 4.12. These RBS spectra were measured shortly after implantation with the fluence 5.2×10^{17}, 1.56×10^{18} and 2.6×10^{18} ions/cm^2, respectively. It can be seen that the Si-deficiency dips of the spectra increase in size as the ion fluence increases. Furthermore, the edges of the Si spectra are shifted towards lower backscattering ion energy. This may be because the amorphous carbon layer was grown on the top surface of the C-ion implanted samples due to the surface segregation of C during irradiation. Thus He^{2+}-ions lose kinetic energy in traversing these carbon front layers. As seen here, the thickness of the carbon layers increases almost linearly with the fluence of the implantation. To make this assumption more clear, Figure 4.13 shows a Raman spectrum of the top carbon layer, which is fitted by double Gaussian distribution. It

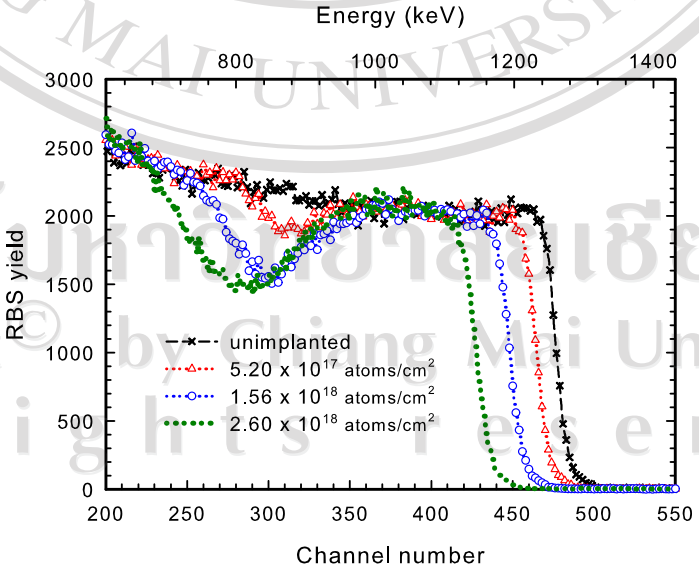

Figure 4.12. 2.1-MeV He^{2+}-ions RBS spectra of as-implanted samples with fluences range from 5.2×10^{17} to 2.6×10^{18} ions/cm^2 at 300-keV.

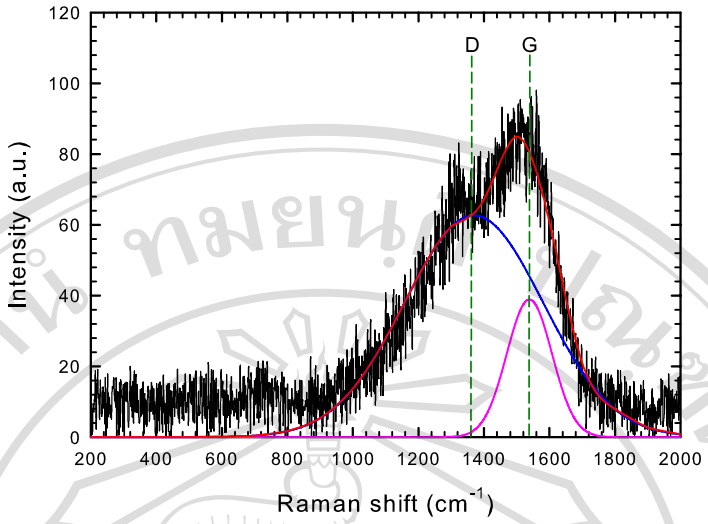

Figure 4.13. Raman spectrum of the top carbon layer on the C-ions implantation sample. The smooth solid lines are the double Gaussian fit.

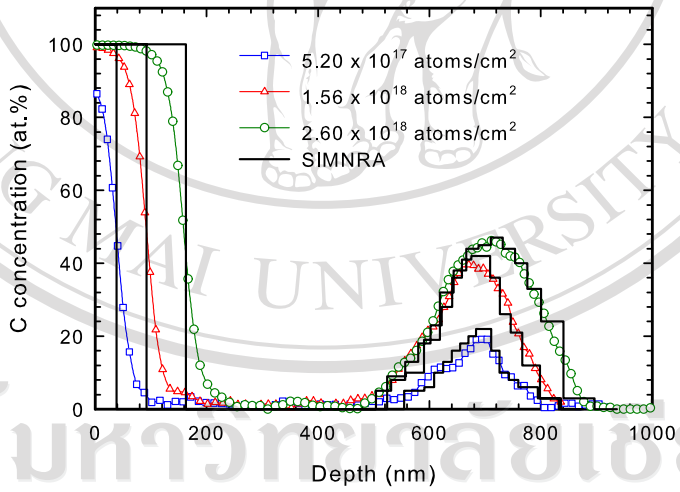

Figure 4.14. Comparison between the calculated depth distributions of the atomic concentration of the C-implanted sample with 300-keV $^{12}C^{+}$-ions and the simulation done by SIMNRA program.

can be seen that the spectrum results in a diamond-like carbon (DLC), which shows broad peaks at around 1540 cm^{-1} and 1370 cm^{-1}, commonly referred to as the G band and D band, respectively.

Nevertheless the C-ion depth profiles were extracted from these RBS spectra, as shown in Figure 4.14, when a top carbon layer covering the surface was taken into account. The simulated depth profiles from SIMNRA code are also included for comparison. It is found that the distributions of the RBS-measured profiles are in good agreement with SIMNRA simulations.

4.4.2 Multi-energy C-ion implantation

Multi-energy C-ion implantations were carried out with two different implantation sequences. The first sequence was implantation from low energy to high energy – namely, 300, 400, 500 and 600 keV – while the second one was vice versa, a method which created a broad synthesized SiC layer. As the fluence for each implantation energy was 7.5×10^{17} ions/cm^2, the summed fluences after each step of implantation were 7.5×10^{17}, 1.5×10^{18}, 2.25×10^{18} and 3.0×10^{18} ions/cm^2, respectively.

Figure 4.15 shows 3-MeV He^{2+}-ions RBS spectra of the as-implanted sample obtained by multiple energy C-ion implantations in the sequence of 300, 400, 500 and 600 keV (known as "increasing sequence"). Figure 4.16 shows the C-ion depth profiles extracted from these RBS spectra. By comparing the measured profiles of the buried C layer with the simulated ones, excellent agreements are observed, thus

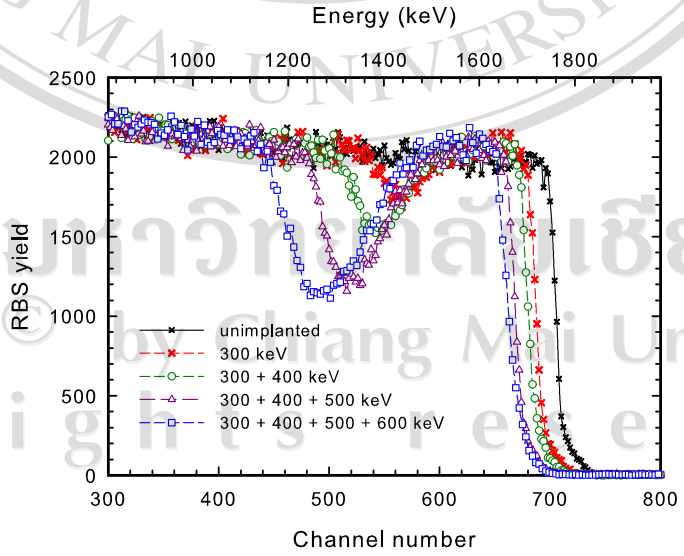

Figure 4.15. 3-MeV He^{2+}-ions RBS spectra of the multiple energy C-ions implanted sample with 300, 400, 500 and 600 keV $^{12}C^{+}$-ions.

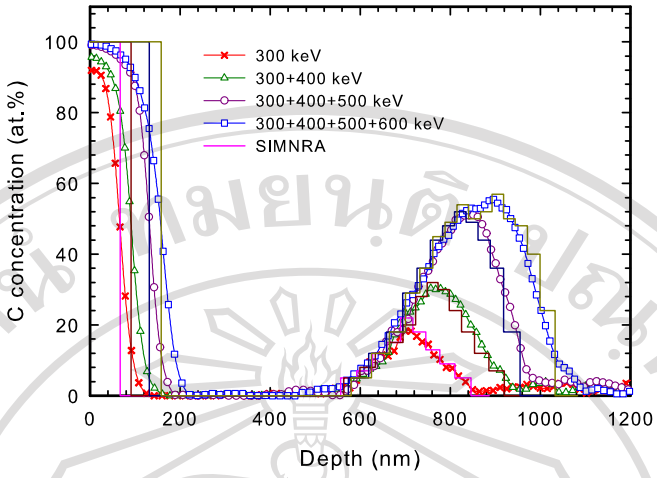

Figure 4.16. Depth distributions of the carbon atomic concentrations of the increasing sequence of C-ions implanted samples which is extracted from the RBS spectra shown in Figure 4.15. The solid lines are their SIMNRA simulations.

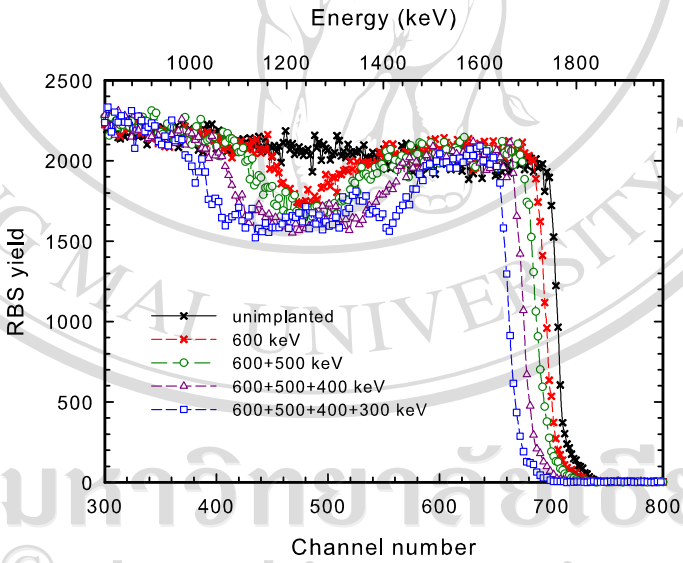

Figure 4.17. 3-MeV He^{2+}-ions RBS spectra of the multiple energy C-ions implanted sample with 600, 500, 400 and 300 keV $^{12}C^{+}$-ions.

demonstrating the measurements using this method to be applicably correct.

Based on the correctness of the technique, C-ion depth profiles of the implantation in reverse sequence (or "decreasing sequence") were also measured, as shown in Figures 4.17 and 4.18. It is seen that the measured C profiles are in ex-

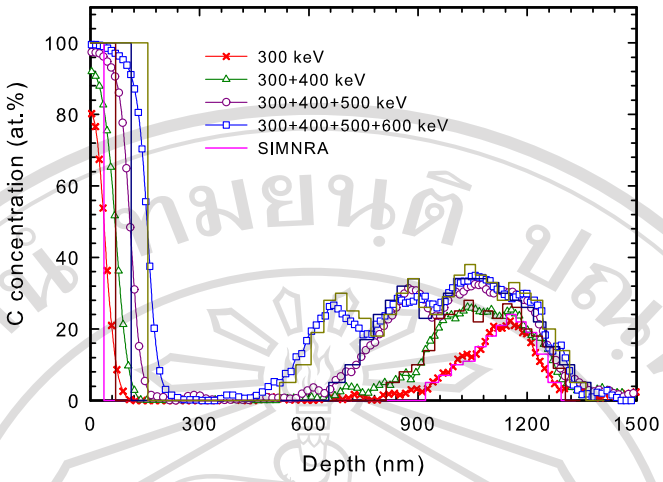

Figure 4.18. Depth distributions of the carbon atomic concentrations of the decreasing sequence of C-ions implanted samples which is extracted from the RBS spectra shown in Figure 4.17. The solid lines are their SIMNRA simulations.

cellent agreement with the simulated ones. As shown in these figures, the buried C profiles are now quite different from those shown in Figure 4.16, featuring rather broadened carbon distributions. This phenomenon was reported, but with little ambiguity, when multiple low-energy C-ion implantation in Si was performed (Ishikawa and Tsuji, 1993). Some mechanisms which might be involved (but not yet confirmed as such) include radiation-enhanced diffusion of carbon, recoiling of carbon ions enhanced by low-energy collisions, and lower stopping for an amorphous structure than for a single crystalline structure of silicon. At any rate, this result provides a useful hint for the synthesis of a SiC layer in Si substrate by C-ion implantation technique. From this analysis, it is demonstrated that this RBS method works in practice even for complicated cases.

4.4.3 Summary

A simple method for non-destructive determining the implantation profile of impurity atoms with a mass number smaller than the target material is presented. The atomic depth profiles are obtained directly from the experimental RBS data in the deficient part of the spectrum from the heavy matrix without any fitting and simulation. The method was demonstrated to work well in a simple, easy and straight forward manner for extracting detailed carbon depth profiles from RBS spectra. We

confirm the correctness of the method by applying to carbon-implanted Si wafers in various conditions. Useful information was obtained with the analyses, such as ion implantation conditions to form stoichiometric and broadened SiC layer in Si.